

OPEN ACCESS

Effect of Duty Cycle on the Lifetime of Single Crystal $\text{LiNi}_{0.5}\text{Mn}_{0.3}\text{Co}_{0.2}\text{O}_2$ /Graphite Lithium-Ion Cells

To cite this article: J. H. Cheng *et al* 2020 *J. Electrochem. Soc.* **167** 130529

View the [article online](#) for updates and enhancements.



244th Electrochemical Society Meeting

October 8 – 12, 2023 • Gothenburg, Sweden

50 symposia in electrochemistry & solid
state science

Abstract submission deadline:
April 7, 2023

Read the call for
papers &
submit your abstract!



Effect of Duty Cycle on the Lifetime of Single Crystal $\text{LiNi}_{0.5}\text{Mn}_{0.3}\text{Co}_{0.2}\text{O}_2$ /Graphite Lithium-Ion Cells

J. H. Cheng,^{1,=} J. E. Harlow,^{1,=} M. B. Johnson,¹ Roby Gauthier,¹ and J. R. Dahn^{1,2,z}

¹Department of Physics and Atmospheric Science, Dalhousie University, Halifax, N.S B3H 4R2, Canada

²Department of Chemistry, Dalhousie University, Halifax, N.S B3H 4R2, Canada

The effects of different duty cycles, involving mixtures of charge-discharge cycling and open-circuit storage segments, on the lifetime of single crystal NMC532/graphite cells were studied. Charge-discharge cycling was performed at C/3 with open circuit storage times of 0, 12, 84, 180 h or 3 months applied at upper cutoff voltages (UCV) of 4.1, 4.2 and 4.3 V. Testing was made at 40 °C for a period of 2.5 years. Cells tested to the same UCV showed similar capacity loss and impedance growth with time, independent of the ratio between the time spent cycling or in storage. Differential voltage analysis showed that the vast majority of the capacity loss stemmed from lithium inventory loss at the negative electrode with little or no loss of active materials. The thickness of the pouch cells after testing increased with the fraction of time spent cycling and the amount of gas generated in the cells increased with fraction of time spent in storage at the UCV. These results show that cycled and stored cells age differently, even though a similar capacity fade rate was observed in the first 2.5 years of cell life, which may cause different failure modes at the end of cell life.

© 2020 The Author(s). Published on behalf of The Electrochemical Society by IOP Publishing Limited. This is an open access article distributed under the terms of the Creative Commons Attribution 4.0 License (CC BY, <http://creativecommons.org/licenses/by/4.0/>), which permits unrestricted reuse of the work in any medium, provided the original work is properly cited. [DOI: 10.1149/1945-7111/abbb0a]



Manuscript submitted July 22, 2020; revised manuscript received September 3, 2020. Published October 1, 2020. *This paper is part of the JES Focus Issue on Selected Papers of Invited Speakers to IMLB 2020.*

Supplementary material for this article is available [online](#)

A knowledge of lithium-ion battery lifetime is critical for their successful deployment in various applications. The main sources of cell aging can be categorized into those stemming from charge-discharge cycling and those stemming from storage. Cycling and storage aging have been extensively studied in combination with other factors such as temperature, current-rate, and state of charge (SoC).^{1–9} However, storage and cycling tests are commonly done separately in order to simplify performance evaluation and use battery charge-discharge equipment most efficiently. However, in a typical use case, cells are often operated in a complex duty cycle with a combination of cycling and storage steps.

In an electric vehicle, the user often operates batteries during the day and stores in the fully or partially charged state at night. Studying the effect of duty cycles that combine cycling and storage will lead to a better understanding of lithium-ion cell aging mechanisms. To our knowledge, combined cycling and storage duty cycles are rarely discussed.^{10–13} Redondo-Iglesias et al. showed that after 120 duty cycles at 60 °C, the larger the fractional storage time, the higher the capacity fade.¹⁴ In terms of time-dependent capacity fade, they built a model, which combined fitting results obtained from pure cycling and pure storage separately to predict the fade of mixed protocols. They showed that, given the same amount of total cycle and storage times, cells given a single long rest after every 7 cycles outperformed those given several short rests between each cycle.¹³ However, the reported testing period was relatively short (<3 months) and failure analysis was not addressed in detail. Therefore, a systematic investigation is needed. Previously, Xia et al., reported the effect of different cycling protocols on capacity loss by using an ultra-high precision charger to cycle cells for around 700 h.¹² One protocol that they called “cycle-store” involved charging to the top of charge and then leaving cells under open circuit conditions for extended times before discharge. They showed that longer times at high voltage (in the cycle-store protocol) resulted in lower Coulombic efficiency and higher charge end-point capacity slippage due to the higher propensity for electrolyte oxidation at high voltage. Here, the effect of storage time in a cycle-store duty cycle on the aging mechanisms of single crystal

$\text{Li}[\text{Ni}_{0.5}\text{Mn}_{0.3}\text{Co}_{0.2}]\text{O}_2$ /artificial graphite pouch cells was studied. This particular chemistry was chosen for this work because the electrodes show very little active mass loss during continuous cycle testing for up to 3 years.¹

Experimental

Pouch cells.—Dry (no electrolyte) and sealed $\text{Li}[\text{Ni}_{0.5}\text{Mn}_{0.3}\text{Co}_{0.2}]\text{O}_2$ (NMC532)/graphite 402035-size pouch cells were obtained from Li-FUN Technology (Xinma Industry Zone, Golden Dragon Road, Tianyuan District, Zhuzhou City, Hunan Province, China, 412000). The cells had a nominal capacity of 240 mAh at 4.3 V. The NMC532 used in these cells was single crystal NMC532 as described by Li et al.¹⁵ with a Ti-based coating as described by Ma et al.¹⁶ The artificial graphite used was Kaijin AML-400 from Kaijin, China. The single side active material electrode loadings were 21.1 mg cm^{−2} for the positive electrode and 12.2 mg cm^{−2} for the graphite negative electrode. The positive and negative electrodes consisted of 94 wt.% and 95.4 wt.% active materials, respectively. The positive electrode was compressed to 3.5 g cm^{−3} and negative electrode was compressed to 1.55 g cm^{−3}. Prior to filling with the designed electrolytes, pouch cells were cut open and dried at 100 °C under vacuum for 14 h to remove residual moisture. Afterwards, pouch cells were filled with 0.85 ml electrolyte in an Ar-filled glove box and sealed with a pouch sealer (MSK-115A Vacuum Sealing Machine, from MTT) under vacuum at a gauge pressure of −90 kPa. Additional information can be found in Harlow et al.¹

Electrolyte.—All the electrolyte solvents and LiPF_6 were battery grade, obtained from Shenzhen Capchem (China) and used as received. Ethylene carbonate (EC), ethyl methyl carbonate (EMC), vinylene carbonate (VC) and ethylene sulfate (DTD) were used in blending the electrolyte. The electrolyte was 1.5 M LiPF_6 EC:EMC 3:7 (by weight) with 2% VC + 1% DTD additives. This particular electrolyte has been promoted by Li et al.¹⁵ and Harlow et al.¹

Testing protocols.—Long-term cycle and storage testing was performed using battery testers from Neware (Shenzhen, China). The particular advantage of these Neware instruments is that they are extremely robust, operating without failure for many years, and are relatively inexpensive so that one can afford to have cells in OCV stand, occupying a charger channel, for the majority of their testing time. All cells were mounted in testing fixtures which applied

⁼These authors contributed equally to this work.

^zE-mail: jeff.dahn@dal.ca

approx. 75 kPa to the electrode stack in order to force any generated gas into the gas bag of the cells, hence maintaining excellent stack pressure. The cycling protocols used are shown in Fig. 1, which indicates duty cycles comprising of cycling and storage segments. The cycling part operated between 3.0 V and three upper cutoff voltages (UCV), including 4.1, 4.2 and 4.3 V, using a C/3 rate at 40 °C. Charging used CCCV mode with a C/20 current cutoff. Between every two cycles, a storage step was performed at top of charge with times including 0, 12, 84 and 180 h, which are denoted as STO0, STO12, STO84 and STO180 duty cycles. A three-month storage result was also extracted from our previous work on the same cell chemistry,¹ denoted as STO3m, which serves as pure storage conditions (cell barcodes in Ref. 1 are 82436–82438). Cells were moved from the Neware cyclers to an ultra high precision cycler¹⁷ at 5, 17 and 30 months for several cycles at C/40 and 40 °C in order to conduct differential voltage (dV/dQ vs Q) analysis.^{18,19} The difference between the average charge voltage and the average discharge voltage, ΔV , was measured and used as a measure of cell internal resistance. Graphs of ΔV vs cycle number or time are used to monitor the stability of cell internal resistance.

Electrochemical impedance spectroscopy (EIS).—The electrochemical impedance spectra of the pouch cells were collected at 5, 12, 17 and 30 month points. A BioLogic VMP3 equipped with three EIS boards was used. All the measurements were performed at 10.0 °C \pm 0.1 °C from 100 kHz to 10 mHz (10 mV input). A temperature of 10 °C was selected to amplify the differences between cells due to changes in charge transfer resistance.²⁰

Gas volume measurement.—The gas production in pouch cells after formation was measured using Archimedes' principle. Each cell was suspended underneath a Shimadzu analytical balance (AUW200D) and weighed while submerged in nano-purified deionized (DI) water (18 M Ω · cm). The produced gas (Δv) in each cell is proportional to the change in apparent cell weight (Δm) that was caused by the buoyant force, as Eq. 1:

$$\Delta v = -\Delta m / \rho \quad [1]$$

where ρ is the density of DI water.

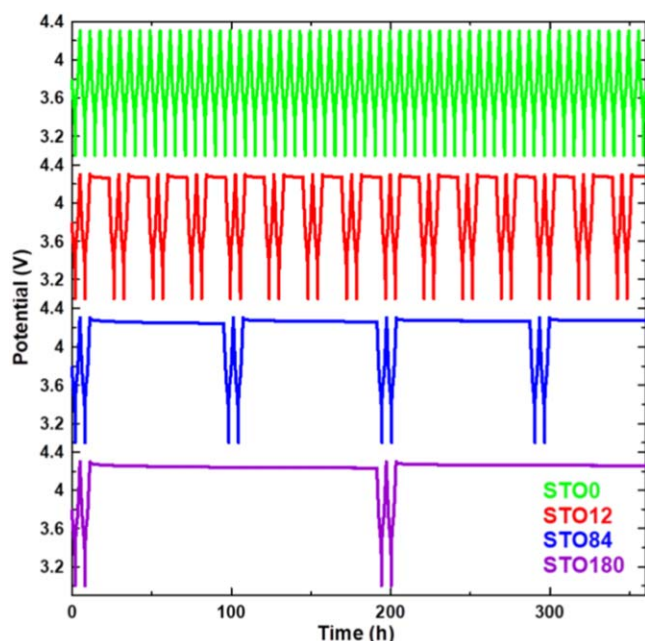


Figure 1. Duty cycles combining two C/3 cycles and 0, 12, 84 or 180-h storage at top of charge (ToC) are denoted as STO0 (green), STO12 (red), STO84 (blue) and STO180 (purple), respectively.

Thickness measurements.—The cell was secured to a flat aluminum stage, and a displacement sensor (Mitutoyo Linear Gage, model 542-132) was used to measure the cell thickness. This linear gage is designed with a spring-loaded displacement pin to minimize noise from inconsistencies in the pouch. The resolution of the gage is 0.5 μ m and the pressure applied by the spring is very minimal, <60 kPa (spec <4.6 N, contact foot area is 78.5 mm²). This measurement was performed at room temperature. The gas bag is still attached to the cell during and after testing so any gas present is pushed to the gas bag and does not affect the thickness measurement.

Ultrasonic transmission mapping.—An ultrasonic battery scanner (UBSC-LD50, Jiangsu Jitri-Hust Intelligent Equipment Technology Co., Ltd.) was employed. A pair of ultrasonic focus transducers (2 MHz frequency, 30 mm focal distance, customized from Shantou Institute of Ultrasonic Instruments Co., Ltd.) were positioned on either side of the cell. Transducers and cells were immersed in low viscosity silicone oil (0.1 cPoise) which serves as an ultrasonic coupling agent. The transducers were installed on a 2-dimensional motion system with a precision of 0.2 mm to perform mechanical progressive scanning. The ultrasonic signal was emitted by a transducer on one side of the cell and received by the transducer on the other side. The driving source was a 200 V pulse signal with a pulse width of 250 ns, matching the 2 MHz ultrasonic transducer used here. The waveform of the transmitted signal was recorded with a collecting card. The peak-to-peak values of received transmission waves were converted into color heat maps to make pseudo color images. This instrument and method are described in greater detail in Ref. 21.

Results and Discussion

Figure 2 shows the capacity and ΔV vs cycle number for cells tested with STO0, STO12, STO84 and STO180 duty cycles at 4.1, 4.2 and 4.3 V. The cells were cycled for 3650 \pm 100 cycles, 1800 \pm 50 cycles, 440 \pm 10 cycles and 220 \pm 5 cycles for the storage times of 0, 12, 84 and 180 h, respectively. For the cells tested to an UCV of 4.1 V, the capacity drops from an initial capacity of 190 mAh to about 160 ~ 170 mAh for the cells with the various duty cycles and ΔV increases by about 0.1 V compared to the minimum ΔV found in the early cycles. Similar behavior is also observed for the 4.2 and

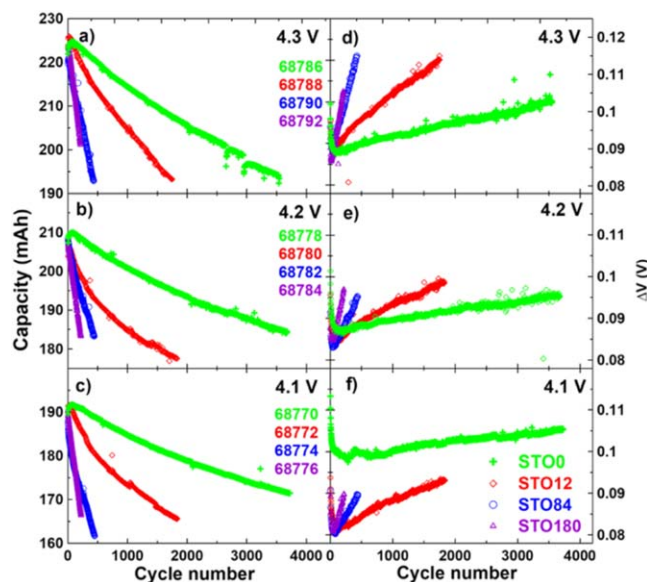


Figure 2. Capacity (a)–(c) and ΔV (d)–(f) vs cycle number for cells tested with STO0, STO12, STO84 and STO180 duty cycles with UCV of 4.1, 4.2 and 4.3 V. All cells were cycled at 40 °C using the duty cycles shown in Fig. 1. The y axis scale in Fig. 2d is different than Figs. 2e and 2f.

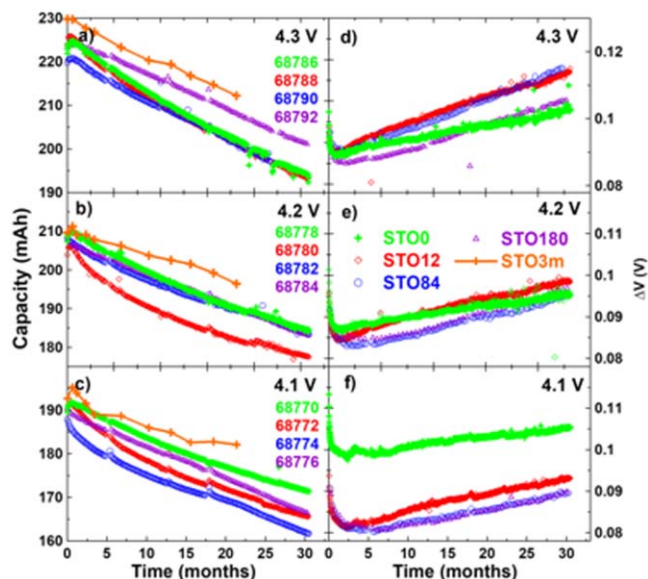


Figure 3. Capacity (a)–(c) and ΔV (d)–(f) vs time for cells tested with STO0, STO12, STO84, STO180 and STO3m duty cycles with UCV of 4.1, 4.2 and 4.3 V. Cells were cycled at 40 °C using the duty cycles shown in Fig. 1, except for the STO3m cells which were evaluated after each 3 month OCV storage period. The y-axis scale in Fig. 3d is different than those in Figs. 3e and 3f.

4.3 V UCV cells. This result clearly shows that the capacity loss and impedance growth don't follow the same curves when plotted vs cycle number.

Figure 3 shows the capacity and ΔV plotted vs testing time up to approximately 30 months for the same cells as Fig. 2. In order to compare to the pure storage case, the STO3m capacity vs time is also included in the plot for 22 months of testing. Note that the reference performance tests for the STO3m cells were performed at 20 °C

(To reiterate—the STO3m cells were stored at 40 °C) so ΔV is higher than for the cycle-store cells and does not fit within the axes of the plot. Figure 3 clearly shows that the cells subjected to STO0, STO12, STO84, STO180 and STO3m duty cycles have very similar capacity decay and ΔV growth vs time.

Figure 4 shows the normalized capacity and normalized ΔV plotted vs time to better compare the small differences between cells. As in Fig. 3, Fig. 4 shows similar capacity fading rates and ΔV growth rate for all the cycle-store cells. However, small but interesting differences are observed: (1) The cells tested with the STO12 duty cycle show the highest rates of capacity loss and ΔV growth, (2) The cells tested with the STO0 duty cycle show the smallest ΔV growth, (3) The ΔV growth rate increases as the UCV increases for all duty cycles. (4) ΔV of the STO3m cell shows a higher growth rate in the first 10 months but flattens out afterwards. The cells with the STO0 duty cycle had the smallest ΔV growth rate presumably because they spent the least fraction of time at high voltage. Since the cells were stored in OCV conditions and since the voltage drops during the storage period as will be discussed later, it is actually difficult to determine which of the STO12, STO84 and STO180 cells is subjected to the most aggressive conditions as far as voltage is concerned.

Figures 4g–4j show the area specific charge transfer resistance, R_{ct} . Here, R_{ct} is taken as the diameter of the low to mid frequency “semicircle” in the EIS spectra shown in Figs. S1 and S2 (available online at stacks.iop.org/JES/167/130529/mmedia). R_{ct} includes effects from both the positive and negative electrodes. Each subplot includes two sets of measurements; one measured at 3.8 V (the lower part) and the other measured at the ToC (the higher part). R_{ct} measured at 3.8 V shows 0 ~ 10% growth over time for cells tested to upper cutoff voltages of 4.1 and 4.2 V using the duty cycles in Fig. 1 and 10 ~ 30% growth for cells tested to 4.3 V. R_{ct} values measured at the ToC are larger than those measured at 3.8 V and appear to show generally a higher growth rate (except for STO0 and STO12 cells at 4.3 V). This phenomena of voltage-dependent resistance growth has been reported in the literature and could relate to the voltage dependent lithium content in the rock-salt layer formed at the cathode surface proposed by Weber et al.²² The results

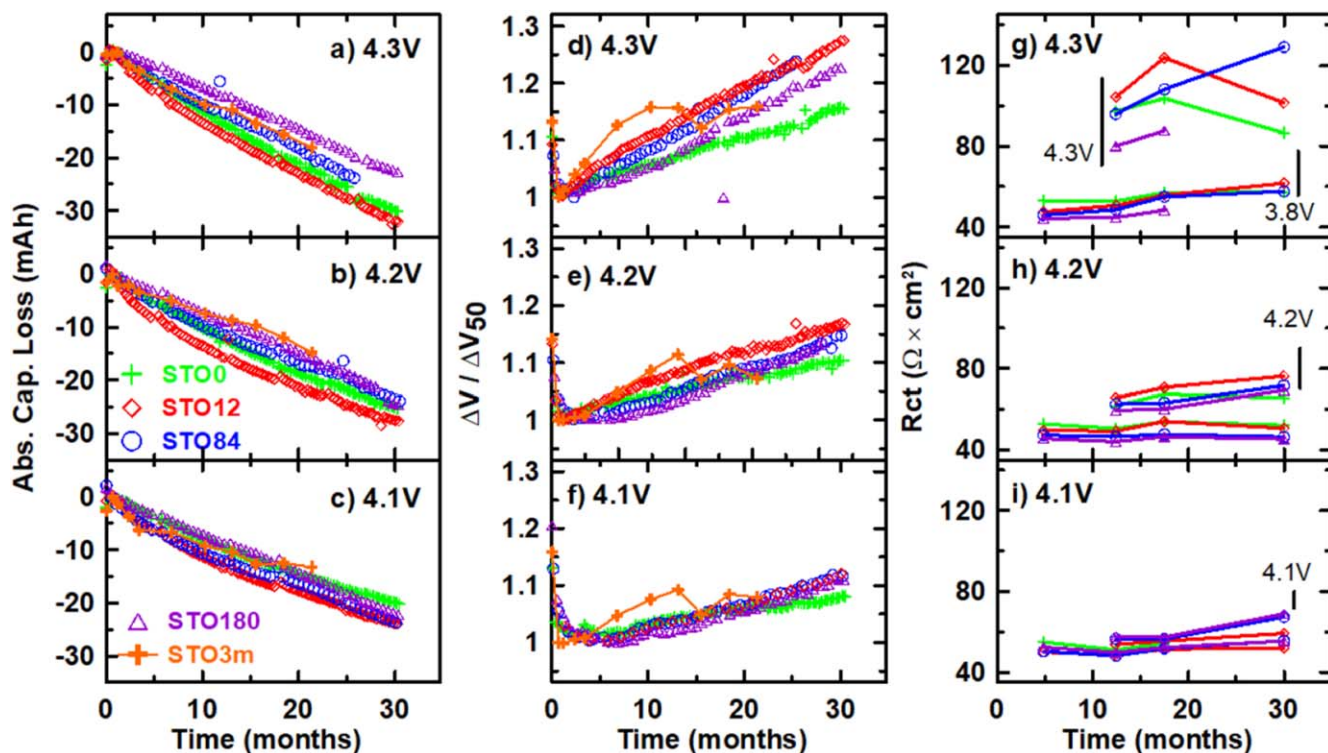


Figure 4. Absolute capacity loss, normalized ΔV and area specific R_{ct} vs time for the cells described by Figs. 2 and 3. EIS spectra for each cell can be found in Supplemental Figs. S1 and S2 and extracted values for R_{ct} can be found in Tables SI and SII.

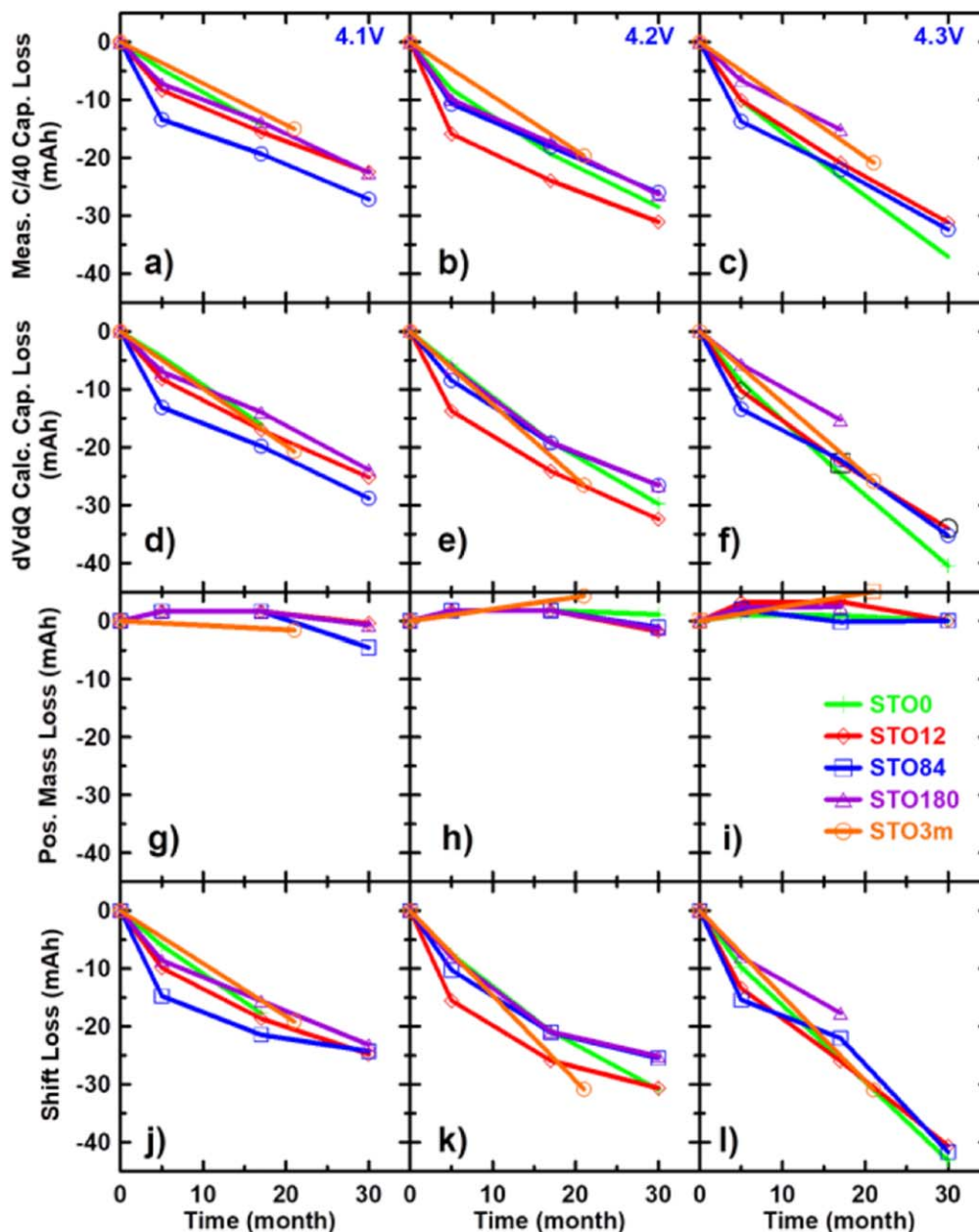


Figure 5. dV/dQ analysis results for the C/40 reference cycles measured periodically at 40 °C. (a)–(c) measured C/40 capacity loss at 4.1, 4.2 and 4.3 V, respectively; (d)–(f) Calculated capacity loss based on dV/dQ analysis at 4.1, 4.2 and 4.3 V, respectively; (g)–(i) Capacity loss due to lithium inventory loss or shift loss at 4.1, 4.2 and 4.3 V, respectively. Note that all the panels have the same y-axis scale. The fits of the measured and calculated dV/dQ vs Q curves are shown in supplemental Figs. S3–S6.

agree with the trends in the ΔV growth shown in Figs. 4d–4f and suggest that the increase of ΔV is mainly controlled by the high voltage region.

Differential voltage analysis (dV/dQ vs Q) was conducted for all cells periodically in order to determine the cell capacity loss mechanism(s). A C/40 RPT cycle at 40 °C was collected at 5, 17 and 30 months for the cells undergoing the STO0, STO12, STO84 and STO180 duty cycles and was collected at 22 months for the STO3m cell. Figure 5 shows the results of the dV/dQ analysis. The format of Fig. 5 is that each column shows results for a duty cycle with the same UCV. The rows in Fig. 5, from bottom to top are capacity loss from lithium inventory or shift loss, capacity loss due to positive active mass loss, calculated capacity loss based on the sum of shift loss and mass loss and measured capacity loss.

Figures 5a, 5d, 5g and 5j show that the shift loss contributes to ~25 mAh capacity loss for the 4.1 V cells and mass loss contributes

less than 5 mAh for all the cells exposed to the duty cycles in Fig. 1 after 30 months of testing. There was about ~20 mAh of shift loss for the STO3m RPT cell after 22-months of testing. Therefore, the calculated capacity loss from dV/dQ analysis is dominated by shift loss and aligns well with the measured capacity loss. The other panels in Fig. 5 show that this same behavior also occurs in the cells cycled and stored at 4.2 and 4.3 V, where the capacity losses after 30 months are between 25 to 30 mAh and 30 to 35 mAh, respectively. In addition, the difference between the C/40 capacity loss of the STO12 cells and the others at 4.2 and 4.3 V is very small unlike the case for the C/3 duty cycles shown in Fig. 4. This suggests that the slightly higher capacity loss that appeared in the STO12 cells has a contribution from impedance growth as evidenced by the higher ΔV growth shown in Figs. 4d and 4e.

Figure 6 shows the results of the thickness (a)–(c) and volume increase (d)–(f) measurements made on the cells after 30 months of

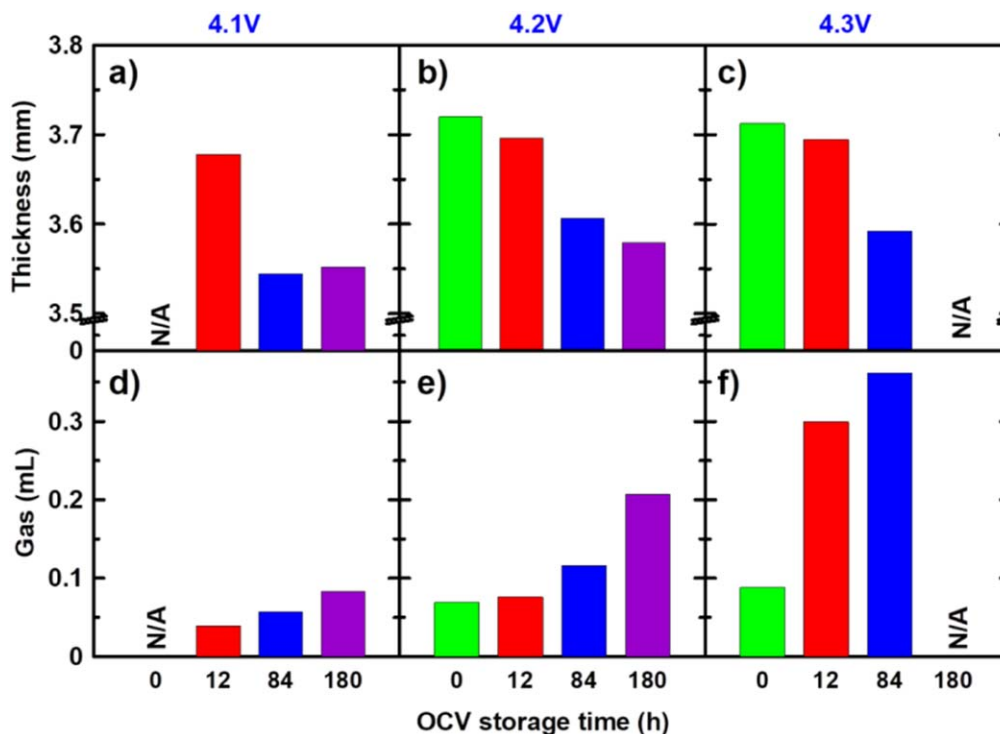


Figure 6. Cell thickness (a)–(c) and volume increase (d)–(f) measurements after 30-months of testing using the duty cycles shown in Fig. 1. The left, middle and right columns are for data collected on cells tested to UCV's of 4.1, 4.2 and 4.3 V, respectively. Due to cell damage results for the STO0 duty cycle at 4.1 V and the STO180 duty cycle at 4.3 V are not available. Only the cell thickness is shown, not the change in cell thickness, because the initial cell thicknesses were not measured (we did not think to do so at the time), however, these machine made cells have initial thicknesses within ± 0.03 mm upon receipt.

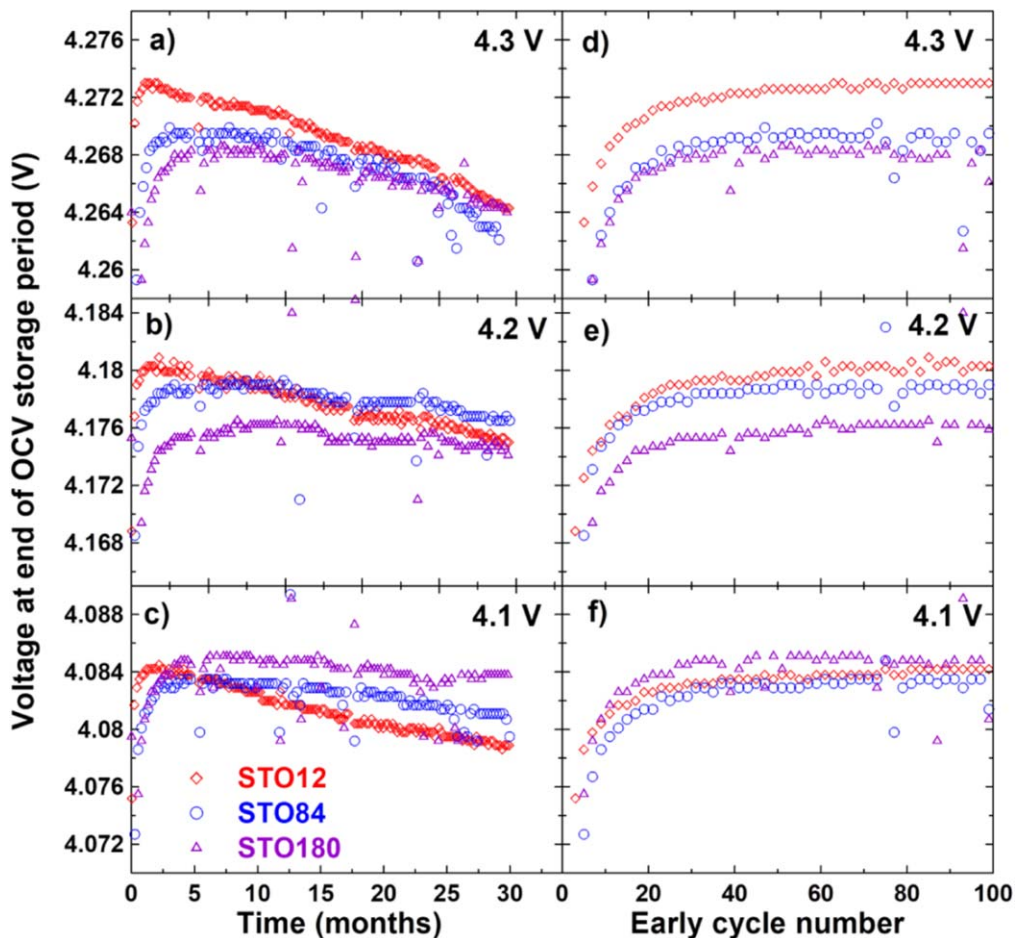


Figure 7. The voltage of the cells at the end of the storage periods plotted (a)–(c) vs time and (d)–(f) vs early cycle number for the cells tested with STO12, STO84 and STO180 duty cycles at UCV's of 4.1, 4.2 and 4.3 V. All cell testing was done at 40 °C.

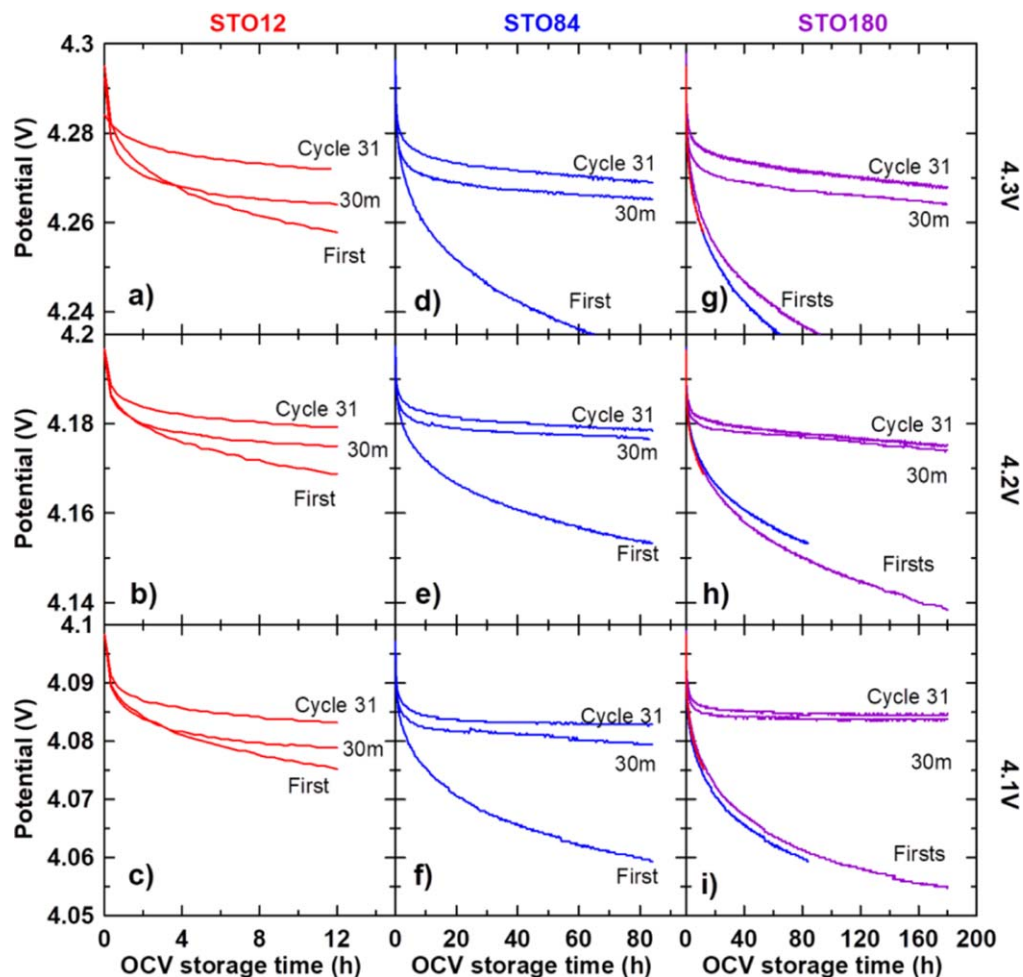


Figure 8. Voltage vs time during storage for the first, 31st and 30-month storage periods for the cells described by Fig. 7. The voltage vs time curves for the first storage period for STO12 (red), STO84 (blue) and STO180 (purple) are superimposed and shown in Figs. 8g–8i.

testing. Results for the cell tested with the STO0 duty cycle at 4.1 V and the cell tested with the STO180 duty cycle at 4.3 V are not available due to damage to the cells. The cell thickness and volume increases show a behavior that has an inverse correlation. The longer the storage time in the duty cycle, the smaller the thickness increase but the larger the volume increase. The volume increase over that predicted from the thickness increase is due to gas production. The volume increase is dependent on the UCV. For example, cells tested with the STO84 duty cycle had 0.06 ml, 0.12 ml and 0.36 ml of volume increase at 4.1, 4.2 and 4.3 V, respectively. A similar dependence of increased gas production with increased UCV can be found in the results from storage experiments on the same cell chemistry in Fig. 21 of Ref. 1. In addition, if we subtract the volume contributed by thickness increase (calculation shown in Supplemental Fig. S7), the differences between the amount of gas produced in the cells tested at the various UCV's is even larger. Although it's a rough estimation, Figs. 6 and S7 demonstrate that the gas production is highly tied to both storage time and the UCV, which are factors that promote electrolyte oxidation.²³ For the thickness increase, the observed behavior of more cycles leading to thicker cells can be explained by considering that during each cycle the electrodes go through a volume expansion/shrinkage which apparently leads to slow irreversible electrode expansion even if it does not lead to enhanced capacity loss in this case.²⁴

The cell voltage at the end of the storage period is plotted vs time for the cells undergoing STO12, STO84 and STO180 duty cycles in Figs. 7a–7c for 4.3, 4.2 and 4.1 UCV's, respectively. The voltage at the end of the storage period first increases with time over the first few months and then gradually decreases over time. This behaviour

can be attributed to slowing down of parasitic reactions at first and increase of impedance afterwards. (Details will be discussed in Fig. 8). Cells tested with the STO12 duty cycle show a steeper slope in the decrease of the cell voltage at the end of the storage period vs time than the other cells do. We believe this is correlated to the higher impedance growth rate shown in Fig. 4. One possible reason for the higher impedance growth rate of cells tested with the STO12 duty cycle is that these cells spend more time including cycle and storage in the higher voltage regions, because they are continually being topped up, and that exacerbates the parasitic reactions.

Figures 7d–7f examine the early cycle dependence of the end of storage voltage for the cells described by Figs. 7a–7c. It is very interesting that all the cells reach their maximum in end of storage voltage around 30 to 60 cycles, even though the times taken to reach the maximum point varies widely due to the wide disparities in the storage times. This may suggest it takes a certain number of volume expansions and contractions of the electrode materials for passivating layers to fully form but this is only speculation.

To further investigate the voltage reached at the end of the storage period (Fig. 7), the voltage vs time during the storage periods was plotted for the first, 31st and 30-month storage period for the cells undergoing STO12, STO84 and STO180 duty cycles in Fig. 8. From the 1st to the 31st cycle, the magnitude of the slope of the voltage-time curve becomes smaller. This voltage drop is caused primarily by parasitic reactions that take place at the positive electrode, because the potential of the lithiated graphite anode is virtually constant on the stage-2/stage-1 plateau.²⁵ Therefore, the reduction of the voltage drop from the 1st to the 31st cycle indicates the slowing down of parasitic reactions. However, from 31st to the

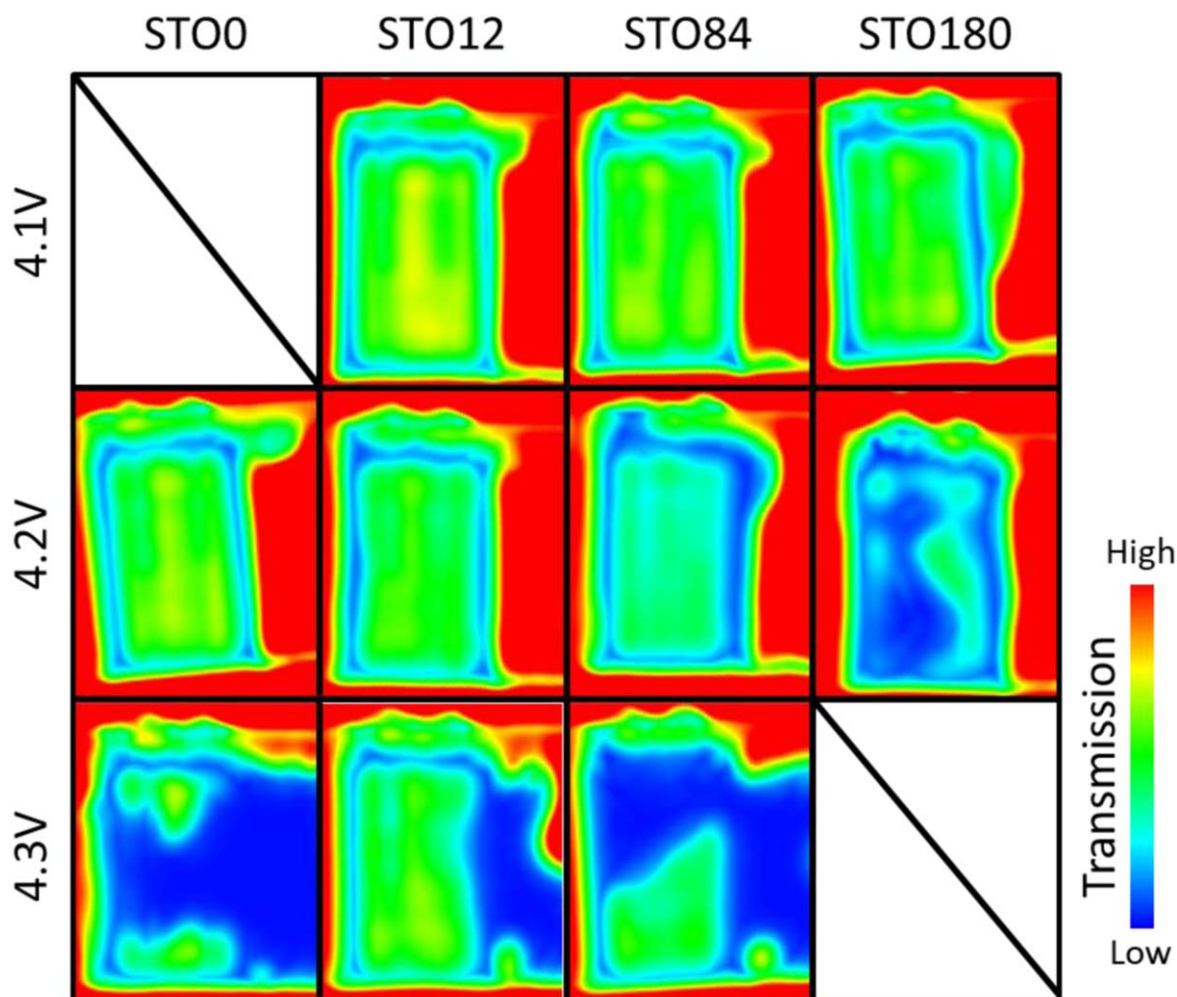


Figure 9. Ultrasonic heat map images taken after 30 months of testing using the duty cycles in Fig. 1. Each image has a size of 38 mm \times 30 mm and the jelly roll size is 28 mm \times 16 mm. The color scale from red (high transmission) to blue (low transmission) is shown on the right. All the cells have a gas bag which extends to the right of the jelly roll in these images.

30-month cycle, although the overall voltage drop increases, that increase appears mostly in the first few hours and the gap between the 31st cycle curve and the 30 month curve remains about the same afterwards. This behavior clearly shows the increase in the voltage drop after the 31st cycle is mainly due to impedance growth but not due to an increase in parasitic reaction rates. The gradually increasing initial voltage drop also is consistent with the growth in ΔV shown in Fig. 4.

Figures 8g–8i show the voltage vs time during storage for the first cycle of the cells tested with STO12, STO84 and STO180 duty cycles superimposed on each other. The curves for the various storage times in the first cycle are virtually on top of each other, but the voltage drops from large to small are STO180, STO84 and STO12. This may explain why the more gas is observed for longer storage time.

To further investigate gas evolution in the pouch cells, ultrasonic transmission mapping was performed. The use of ultrasonic and acoustic emission spectroscopy to inspect the integrity of Si-containing electrodes in pouch cells has been reported.^{26,27} However, spatial resolution across an entire cell is rarely reported.²⁸ Here, we spatially resolved the ultrasonic transmission signal through the pouch cells as described in the experimental section after 30-months of cycling and storage according to the duty cycles in Fig. 1. High-to-low transmission is shown in Fig. 9 using a red-to-blue heat map, indicating a dense-to-loose structure, i.e. good transmission to poor transmission, on each acquired point. As shown in Ref. 21, an electrolyte-filled and degassed cell has excellent transmission but if there is insufficient electrolyte or the formation of

gas, the ultrasonic wave propagation in these conditions is severely depressed and we observe very poor transmission. Figure 9 shows that for the cells tested with STO12, STO84 and STO180 duty cycles at 4.1 V, the jelly rolls all display green and yellow colors, which represents a dense electrode stack. It also indicates the health of the cell is good: no electrode drying and little gas formation. A blue ring is observed bordering the jelly roll/pouch pocket and this may be explained by the fact that the jelly roll is oval while the pouch pocket is square in shape. If all of the electrolyte is wetted inside the jelly roll, what would occur at the pocket edges is a small vacuum void and it was shown this very negatively affects sound transmission. When the UCV increases to 4.2 V, the blue region at the edge of jelly roll gradually expands from STO00 to STO12 to STO84 and covers most of jelly roll in the STO180 cell. This behavior can be attributed to the progressive formation of gas in the pouch cell. Figure 9 shows that the cells tested to 4.3 V display a solid blue color (part of the gas was expelled to the gas bag for STO12 and STO84 cells) indicative of more gas. The results in Fig. 9 align well with the gas volume measurements shown in the Fig. 6.

Conclusions

Single crystal $\text{Li}[\text{Ni}_{0.5}\text{Mn}_{0.3}\text{Co}_{0.2}]\text{O}_2$ (NMC532)/graphite pouch cells were used to study the capacity fading and aging behavior of cells subjected to combined cycling and storage duty cycles at 40 °C. It was found that the capacity loss for various storage times from 0, 12, 84, 180 h and 3 months between cycles is time-dependent, not

cycle-dependent. All these cells showed very similar capacity loss over the 30-month testing with only slightly higher capacity loss and impedance growth for cells that had the 12 h storage periods (the STO12 duty cycle in Fig. 1). The lithium inventory loss or shift loss was found to be the primary cause for the capacity loss through differential voltage analysis. More gas production was observed after 30-months of testing for cells that had longer storage times, thus exposing them to higher voltages for longer periods. Cells that underwent more charge-discharge cycles had greater thickness growth. These differences may lead to different failure modes at the end of life, such as cell thickness increase (many cycles) or bulging (gas generation) for pouch cells. For cylindrical cells gassing can lead to activation of the current interrupt devices or even venting while electrode thickening can lead to pore clogging or separator collapse. These factors should be taken into consideration when considering duty cycles that may be used by particular cell designs.

Acknowledgments

This work was supported by the NSERC/Tesla Canada Industrial Research Chairs program. We also acknowledge Zhe Deng, Y. Shen and Y. Huang (State Key Laboratory of Material Processing and Die & Mould Technology, School of Materials Science and Engineering, Huazhong University of Science and Technology, Wuhan, Hubei, China) for providing the ultrasonic testing machine.

ORCID

J. E. Harlow  <https://orcid.org/0000-0002-3928-2573>

M. B. Johnson  <https://orcid.org/0000-0001-6445-2813>

Roby Gauthier  <https://orcid.org/0000-0003-4033-8578>

J. R. Dahn  <https://orcid.org/0000-0002-6997-2436>

References

1. J. E. Harlow et al., *J. Electrochem. Soc.*, **166**, A3031 (2019).
2. P. Ramadass, B. Haran, R. White, and B. N. Popov, *J. Power Sources*, **112**, 606 (2002).
3. M. Broussely, P. Biensan, F. Bonhomme, P. Blanchard, S. Herreyre, K. Nechev, and R. J. Staniewicz, *J. Power Sources*, **146**, 90 (2005).
4. M. Ecker, N. Nieto, S. Käbitz, J. Schmalstieg, H. Blanke, A. Warnecke, and D. U. Sauer, *J. Power Sources*, **248**, 839 (2014).
5. J. Schmalstieg, S. Käbitz, M. Ecker, and D. U. Sauer, *J. Power Sources*, **257**, 325 (2014).
6. P. Keil and A. Jossen, *J. Electrochem. Soc.*, **164**, A6066 (2016).
7. P. Keil and A. Jossen, *Journal of Energy Storage*, **6**, 125 (2016).
8. F. Leng, C. M. Tan, and M. Pecht, *Sci. Rep.*, **5**, 12967 (2015).
9. Y. Zhang, R. Xiong, H. He, X. Qu, and M. Pecht, *Appl. Energy*, **255**, 113818 (2019).
10. M. Ben-Marzouk, A. Chaumond, E. Redondo-Iglesias, M. Montaru, and S. Pelissier, *World Electric Vehicle Journal*, **8**, 388 (2016).
11. S. Grolleau, I. Baghdadi, P. Gyan, M. Ben-Marzouk, and F. Duclaud, *World Electric Vehicle Journal*, **8**, 339 (2016).
12. J. Xia, M. Nie, L. Ma, and J. R. Dahn, *J. Power Sources*, **306**, 233 (2016).
13. E. Redondo-Iglesias, P. Venet, and S. Pelissier, *Batteries*, **6**, 14 (2020).
14. E. Redondo-Iglesias, P. Venet, and S. Pelissier, *Microelectron. Reliab.*, **88–90**, 1212 (2018).
15. J. Li, H. Li, W. Stone, S. Glazier, and J. R. Dahn, *J. Electrochem. Soc.*, **165**, A626 (2018).
16. L. Ma et al., *ACS Appl. Energy Mater.*, **1**, 7052 (2018).
17. T. M. Bond, J. C. Burns, D. A. Stevens, H. M. Dahn, and J. R. Dahn, *J. Electrochem. Soc.*, **160**, A521 (2013).
18. I. Bloom, A. N. Jansen, D. P. Abraham, J. Knuth, S. A. Jones, V. S. Battaglia, and G. L. Henriksen, *J. Power Sources*, **139**, 295 (2005).
19. H. M. Dahn, A. J. Smith, J. C. Burns, D. A. Stevens, and J. R. Dahn, *J. Electrochem. Soc.*, **159**, A1405 (2012).
20. A. S. Keefe, S. Buteau, I. G. Hill, and J. R. Dahn, *J. Electrochem. Soc.*, **166**, A3272 (2019).
21. Z. Deng, Z. Huang, Y. Shen, Y. Huang, H. Ding, A. Luscombe, M. Johnson, J. E. Harlow, R. Gauthier, and J. R. Dahn, *Joule*, **4**, 2017 (2020).
22. R. Weber, A. J. Louli, K. P. Plucknett, and J. R. Dahn, *J. Electrochem. Soc.*, **166**, A1779 (2019).
23. L. E. Downie, S. R. Hyatt, and J. R. Dahn, *J. Electrochem. Soc.*, **163**, A35 (2016).
24. A. J. Louli, L. D. Ellis, and J. R. Dahn, *Joule*, **3**, 745 (2019).
25. N. N. Sinha, A. J. Smith, J. C. Burns, G. Jain, K. W. Eberman, E. Scott, J. P. Gardner, and J. R. Dahn, *J. Electrochem. Soc.*, **158**, A1194 (2011).
26. K. Rhodes, N. Dudney, E. Lara-Curzio, and C. Daniel, *J. Electrochem. Soc.*, **157**, A1354 (2010).
27. A. Tranchot, H. Idrissi, P.-X. Thivel, and L. Roué, *J. Power Sources*, **330**, 253 (2016).
28. J. B. Robinson, M. Maier, G. Alster, T. Compton, D. J. L. Brett, and P. R. Shearing, *Phys. Chem. Chem. Phys.*, **21**, 6354 (2019).